

---

# Neural Fields with Hard Constraints of Arbitrary Differential Order

---

**Fangcheng Zhong**  
University of Cambridge

**Kyle Fogarty**  
University of Cambridge

**Param Hanji**  
University of Cambridge

**Tianhao Wu**  
University of Cambridge

**Alejandro Sztrajman**  
University of Cambridge

**Andrew Spielberg**  
Harvard University

**Andrea Tagliasacchi**  
Simon Fraser University

**Petra Bosilj**  
University of Lincoln

**Cengiz Oztireli**  
University of Cambridge

## Abstract

While deep learning techniques have become extremely popular for solving a broad range of optimization problems, methods to enforce hard constraints during optimization, particularly on deep neural networks, remain underdeveloped. Inspired by the rich literature on meshless interpolation and its extension to spectral collocation methods in scientific computing, we develop a series of approaches for enforcing hard constraints on neural fields, which we refer to as *Constrained Neural Fields* (CNF). The constraints can be specified as a linear operator applied to the neural field and its derivatives. We also design specific model representations and training strategies for problems where standard models may encounter difficulties, such as conditioning of the system, memory consumption, and capacity of the network when being constrained. Our approaches are demonstrated in a wide range of real-world applications. Additionally, we develop a framework that enables highly efficient model and constraint specification, which can be readily applied to any downstream task where hard constraints need to be explicitly satisfied during optimization. – source code will be made publicly available. <https://cnf2023.netlify.app/>

## 1 Introduction

Deep neural networks serve as universal function approximators [10] and have achieved tremendous success across a wide variety of tasks. Gradient-based learning algorithms enable optimizing the parameters of networks to approximate any desired model. However, despite the existence of numerous advanced optimization algorithms, the issue of enforcing strict equality constraints during training has not been sufficiently addressed. Constrained optimization has a broad spectrum of real-world applications. For example, in trajectory optimization ([38][Chapter 10], and, *e.g.*, [4, 29]), the agent poses at the start, end, and potentially intermediate steps are to be explicitly enforced. In signal representation, it is desirable for the continuous model to interpolate the discrete samples [22]. In physics, the models of interest must comply with fundamental physical principles [14, 27].

Applying traditional solvers for nonlinear constrained optimization, such as SQP [25], to neural networks can be nontrivial. Since traditional methods express constraints as a function of learnable parameters, this formulation becomes extremely high-dimensional, nonlinear, and non-convex in the case of neural networks. As the number of parameters grows, the complexity increases substantially.

Other solutions for deep neural networks may encounter issues related to system conditioning, memory consumption, and network capacity when subject to constraints [20].

In this work, we consider the following constrained optimization problem:

$$\arg \min_{\theta} \mathcal{L}(f_{\theta}; \theta) \quad \text{s.t.} \quad \mathcal{F}[f_{\theta}](\mathbf{x}) = g(\mathbf{x}) \quad \forall \mathbf{x} \in \mathcal{S}, \quad (1)$$

where  $f_{\theta}$  is a parametric model with learnable parameters  $\theta$ ; and  $\mathcal{F}$  is a linear operator<sup>1</sup> that transforms  $f$  into another function  $\mathcal{F}[f]$  which has the same input and output dimensions as  $f$ . Common examples of valid operators  $\mathcal{F}$  include the identity map, integration, partial differentiation of any order, and many composite operations that involve differentiation, such as Laplacian, divergence, and advection operators.  $\mathcal{F}$  can represent a broad class of constraints on the function  $f$  in real-world applications. Enforcement of multiple constraints, expressed as different operators on  $f$ , is also possible. In practice, one typically does not have access to (or require) a closed-form expression of  $g$ , but rather the evaluation of  $g$  on a set  $\mathcal{S}$  of discrete samples of  $\mathbf{x}$ . In this work, we focus on equality constraints, as inequality constraints can be more easily satisfied through heavy regularization or a judicious choice of the activation function.

Our solution draws inspiration from meshless interpolation [6], and its extension to spectral collocation methods [7] in the scientific computing literature. These methods model a parametric function as a *linear sum of basis functions*. By computing the weights of the bases, hard constraints on the local behavior of the function at the *collocation points*, where the constraints need to be satisfied, are enforced accordingly. However, the selection of the basis functions also determines the inductive bias of the model, i.e., the behavior of the function outside the collocation points. Our perspective is to formulate the problem of constrained optimization as a *collocation problem with learnable inductive bias*. Instead of using a set of fixed basis functions, we allow each basis function to have additional learnable parameters. While the weights of the basis functions are used to enforce constraints, other learnable parameters are optimized via a training loss to match the optimal inductive bias.

With this formulation of the problem, we demonstrate a series of approaches for enforcing hard constraints in the form of Eq. 1 onto a neural field, i.e., a parametric function modeled as a neural network that takes continuous coordinates as input. In theory, we can formulate basis functions from existing neural fields of any architecture and enforce constraints. Nevertheless, certain network architectures may encounter difficulties when the number of collocation points or the order of differentiation increases. To tackle these challenges, we propose specific network designs and training strategies, and demonstrate their effectiveness in several real-world applications spanning physics, signal representation, and geometric processing. Finally, we develop a PyTorch framework for the highly efficient adoption of Constrained Neural Fields (CNF), which can be applied to any downstream task requiring explicit satisfaction of hard constraints during optimization.

In summary, our work makes the following key contributions:

- We introduce a novel approach for enforcing linear operator constraints on neural fields;
- We propose specific model representations and training strategies to address various challenges that may arise within the problem context;
- Our framework is effective across a wide range of real-world problems; in particular, CNF:
  - achieves state-of-the-art performance in learning material appearance representation.
  - is the first that can enforce an exact normal constraint on a neural implicit field.
  - improves the performance of the Kansa method [18], a meshless partial differential equation (PDE) solver, when applied to irregular input grids.

## 2 Related Work

Applying constraints to a deep learning model has been a long-standing problem. Numerous studies have aimed to enforce specific properties on neural networks. For instance, sigmoid and softmax activation functions are used to ensure that the network output represents a valid probability mass function. Convolutional neural networks (CNNs) were introduced to address translation invariance. Pointnet [30] was proposed to achieve permutation invariance. POLICE [3] was introduced to enforce

<sup>1</sup>While our approach can be theoretically extended to nonlinear operators, we focus on linear ones due to the efficiency of linear solvers and GPU vectorization.

affine properties on the network. However, these works were not specifically designed to handle strict and general-form equality constraints. There are also studies that train a multilayer perceptron (MLP) [34, 37] or neural basis functions [8, 43] with a regression loss to approximate the equality constraints through overfitting. However, in those works, strict adherence to hard constraints is rarely guaranteed. DC3 [12] is the first work that can enforce general equality constraints onto deep learning models by selecting a subset of network parameters for constraint enforcement and utilizing the remaining parameters for optimization. However, this approach cannot offer a theory or guidance regarding the existence of a solution when selecting a random subset of the network. In contrast, our method rigorously analyzes and guarantees the existence of a solution. Linearly constrained neural networks [17] can also explicitly satisfy linear operator constraints, but their method only applies to the degenerate case where  $g(x)$  is zero everywhere. Neural kernel fields (NKF) [41] employs a design of kernel basis functions similar to ours to solve constrained optimization problems in geometry, but their method cannot accommodate strict higher-order constraints. Their use of a dense matrix also cannot scale up to accommodate a large number of constraints, due to limitations in processor memory. A concurrent work, PDE-CL [26], utilizes a constrained layer to solve partial differential equations as a constrained optimization problem. We demonstrate that a constrained layer may not be the ideal design choice for basis functions and propose alternative solutions. In fact, our approach can be seen as a *generalization* of NKF and PDE-CL. While seemingly unrelated, both works approach constrained optimization problems by leveraging the weights of basis functions to enforce constraints. They differ only in the design of the basis and the optimization function. Finally, there has been substantial development in implicit layers [13] that can enforce equality constraints between the layer’s input and output. However, this approach is not specifically designed for constraints over the entire network, although it can be potentially incorporated into our method to facilitate computation.

### 3 Method

At the core of our approach is the representation of a neural field  $f(\cdot) : \mathbb{R}^M \mapsto \mathbb{R}^N$  as a linear sum of basis functions, as with the collocation methods:

$$f(\mathbf{x}) = \sum_i \beta_i \odot \Psi_i(\mathbf{x}), \quad (2)$$

where each  $\Psi_i(\cdot) : \mathbb{R}^M \mapsto \mathbb{R}^N$  is a basis function that can be represented as any parametric function with learnable parameters (e.g., polynomials, neural networks);  $\beta_i \in \mathbb{R}^N$  is the weight of the  $i$ -th basis; and  $\odot$  indicates the Hadamard product.

#### 3.1 Constrained Optimization

Consider  $\mathcal{S} := \{\mathbf{x}_i\}_{i=1}^I$ , a set of  $I$  constraint points such that  $\mathcal{F}[f](\mathbf{x}_i) = g(\mathbf{x}_i), \forall i$  where the ground truth value of  $g(\mathbf{x}_i)$  is accessible. Using the neural basis representation (2), and assuming that  $\mathcal{F}$  is linear and  $\mathcal{F}[\Psi_i]$  is well-defined for all  $i$ , the following needs to hold for the constraints:

$$\mathcal{F}[f](\mathbf{x}) = \mathcal{F}\left[\sum_i \beta_i \odot \Psi_i\right](\mathbf{x}) = \sum_i \beta_i \odot \mathcal{F}[\Psi_i](\mathbf{x}) = g(\mathbf{x}), \forall \mathbf{x} \in \mathcal{S}. \quad (3)$$

Eq. 3 is a *collocation equation* in the context of spectral collocation methods for solving differential and integral equations [9, 1]. These constraints can be explicitly satisfied by defining  $I$  basis functions and solving Eq. 3 for their weights. For a linear  $\mathcal{F}$ , we can expand Eq. 3 into batched matrix form:

$$\underbrace{\begin{bmatrix} \mathcal{F}[\Psi_1](\mathbf{x}_1) & \mathcal{F}[\Psi_2](\mathbf{x}_1) & \cdots & \mathcal{F}[\Psi_I](\mathbf{x}_1) \\ \mathcal{F}[\Psi_1](\mathbf{x}_2) & \mathcal{F}[\Psi_2](\mathbf{x}_2) & \cdots & \mathcal{F}[\Psi_I](\mathbf{x}_2) \\ \vdots & \vdots & \ddots & \vdots \\ \mathcal{F}[\Psi_1](\mathbf{x}_I) & \mathcal{F}[\Psi_2](\mathbf{x}_I) & \cdots & \mathcal{F}[\Psi_I](\mathbf{x}_I) \end{bmatrix}}_{\mathbf{A}_f} \begin{bmatrix} \beta_1 \\ \beta_2 \\ \vdots \\ \beta_I \end{bmatrix} = \begin{bmatrix} g(\mathbf{x}_1) \\ g(\mathbf{x}_2) \\ \vdots \\ g(\mathbf{x}_I) \end{bmatrix}. \quad (4)$$

There are in total  $N$  such matrix equations to solve, each corresponding to an output dimension of  $f$  if  $N > 1$ . We denote the matrix as  $\mathbf{A}_f$  for reference. As long as we apply a differentiable linear solver that provides valid gradients to compute the weights, the neural basis representation (Eq. 2) can be integrated with any optimization loss  $\mathcal{L}(f_\theta; \theta)$  while the constraints are always explicitly satisfied. This approach can also be extended to multiple linear operator constraints, indexed by  $j$ :

$$\mathcal{F}_j[f](\mathbf{x}) = g_j(\mathbf{x}), \forall \mathbf{x} \in \mathcal{S}_j, \quad (5)$$

where  $S_j$  indicates the set of points  $\mathbf{x}$  where the values of  $\mathcal{F}_j[f](\mathbf{x})$  are constrained. Note that  $S_j$  corresponding different operator constraints can have repeated  $\mathbf{x}$  elements. For example, to constrain  $\nabla f(\mathbf{x})$  where  $\mathbf{x} \in \mathcal{S} \subseteq \mathbb{R}^M$ , a partial differentiation operator needs to be specified for each of the  $M$  partial derivatives at the same point  $\mathbf{x}$ . These constraints can be explicitly satisfied by defining  $\sum_j |S_j|$  basis functions and computing their weights by solving the batched matrix equation:

$$\begin{bmatrix} \mathcal{F}_1[\Psi_1](\mathbf{x}_1^1) & \mathcal{F}_1[\Psi_2](\mathbf{x}_1^1) & \cdots \\ \mathcal{F}_1[\Psi_1](\mathbf{x}_2^1) & \mathcal{F}_1[\Psi_2](\mathbf{x}_2^1) & \cdots \\ \vdots & \vdots & \ddots \\ \mathcal{F}_2[\Psi_1](\mathbf{x}_1^2) & \mathcal{F}_2[\Psi_2](\mathbf{x}_1^2) & \cdots \\ \mathcal{F}_2[\Psi_1](\mathbf{x}_2^2) & \mathcal{F}_2[\Psi_2](\mathbf{x}_2^2) & \cdots \\ \vdots & \vdots & \ddots \end{bmatrix} \begin{bmatrix} \beta_1^1 \\ \beta_2^1 \\ \vdots \\ \beta_1^2 \\ \beta_2^2 \\ \vdots \end{bmatrix} = \begin{bmatrix} g_1(\mathbf{x}_1^1) \\ g_1(\mathbf{x}_2^1) \\ \vdots \\ g_2(\mathbf{x}_1^2) \\ g_2(\mathbf{x}_2^2) \\ \vdots \end{bmatrix}, \quad (6)$$

where  $\mathbf{x}_n^j$  indicates the  $n$ -th point in  $S_j$ . Note that, when employing general solvers such as SQP and DC3 [12], which formulate the constraint as a function of arbitrary network parameters, the constraint in the form of Eq. 1 could become *nonlinear* even if  $\mathcal{F}$  is linear. Our formulation reduces the problem’s complexity, which allows us to determine whether a solution to Eq. 4 and Eq. 6 exists.

### 3.2 Neural Basis Functions

To construct a set of basis functions from an existing neural field, we consider a few approaches.

**Independent basis** The most straightforward method is to specify a *separate* neural field for each basis. This method is the most expressive but can only be used with a small number of constraints, as we demonstrate in the optical trajectory optimization example (see Sec. 4.1). This is because the number of networks, and trainable parameters, increase linearly with the number of constraints. A bigger concern is the quadratic growth in the size of the matrix  $\mathbf{A}_f$ . As a result, even high-end processors are guaranteed to run out of memory when working with a large number of constraints.

**Constraint basis** We can directly use the last hidden layer of a multi-layer perceptron (MLP) as the basis and compute the weight of each node to enforce the constraints. This strategy has been referred to as a *constraint layer* in concurrent work [26]. The size of the network, excluding the hidden layer, does not increase as the number of constraints grows. However, this approach may lead to linearly-dependent basis functions, resulting in the matrix  $\mathbf{A}_f$  being singular or having a *large condition number*. This can lead to a significant error bound in the solution vector.

**Hypernetwork basis** The third approach is to generate the parameters of a neural field using a *hypernetwork* [16]. The input to the hypernetwork is a one-hot encoding of length equal to the number of bases. The hypernetwork ensures that the network size does not increase with the number of basis functions. Nonetheless, the quadratic growth in the size of the matrix remains an issue for both the constraint and the hypernetwork bases.

In several empirical studies, we found that the aforementioned approaches hinder the network’s capacities when subjected to hard constraints. We also encountered difficulties reducing the condition number; see [Supplementary](#).

**Kernel basis** As a result, we propose several variants of a *neural kernel function* as a special design of basis functions:

$$\Psi_i(\mathbf{x}) = \kappa(\phi(\mathbf{x}_i), \phi(\mathbf{x})), \quad (7)$$

where  $\phi(\cdot)$  is a neural encoder that maps  $\mathbf{x}$  into a feature space;  $\kappa(\cdot, \cdot)$  is a kernel function that measures the similarity between two points in the feature space;  $\mathbf{x}_i$  is the  $i$ -th constraint point, which we refer to as an *anchor point*. With this design, the higher-dimensional feature space bolsters the learning capacity of the basis function. The size of parameters in the network also does not grow with the number of constraints. If  $\kappa(\cdot, \cdot)$  is a dot-product kernel, Eq. 7 becomes the same basis function used in NKf [41]. However, we empirically found that a Gaussian kernel better promotes linear independence of basis functions, while still preserving sufficient learning capacity; see [Supplementary](#).

**Hypernetwork kernel basis** One drawback of the kernel basis function is that only one constraint can be applied to each anchor point. For example, one cannot enforce constraints on both the value of  $f(\mathbf{x})$  and its gradient  $\nabla f(\mathbf{x})$  at the same anchor point, as it would result in *repeated* basis functions  $\Psi_i \equiv \Psi_j \equiv \kappa(\phi(\mathbf{x}_{\text{anchor}}), \phi(\mathbf{x}))$  and thus an ill-conditioned system; see [Supplementary](#) for math details. For multiple constraints at repeated anchor points, we propose a *hypernet kernel function*:

$$\Psi_i(\mathbf{x}) = \kappa(\phi_i(\mathbf{x}_i), \phi_i(\mathbf{x})), \quad (8)$$

where the weights of  $\phi_i$  are controlled by a hypernetwork conditioned on the anchor point  $\mathbf{x}_i$ . This hypernet construction of the encoder ensures that the network would not have repeated basis functions and the number of network parameters does not grow with the number of basis functions.

**Hybrid kernel basis** Central to our approach is the construction and inversion of a linear system, the size of which grows quadratically with the number of constraint points. While using a Gaussian kernel can promote sparsity, it becomes challenging to select a proper bandwidth ( $\sigma^2$ ) to explicitly control the number of nonzero elements since the kernel operates in the feature space rather than the original domain. To overcome this limitation, we propose a *hybrid kernel function*:

$$\Psi_i(\mathbf{x}) = \kappa(\phi_i(\mathbf{x}_i), \phi_i(\mathbf{x})) \kappa_G(\mathbf{x}_i, \mathbf{x}), \quad (9)$$

where  $\kappa_G$  is some compactly supported kernel function (such as a truncated Gaussian kernel). By careful selection of the function  $\kappa_G$ , the linear system to be solved for each  $\mathbf{x}$  can be made sparse, breaking the quadratic dependency on the number of constraint points.

### 3.3 Training Strategies

**Regularization** Depending on the application, we recommend incorporating an additional loss term to regularize the condition number of the matrix  $\mathbf{A}_f$  during optimization. A low condition number corresponds to a reduced level of matrix singularity and a smaller error bound in the solution vector, which is crucial for satisfying hard constraints.

**Transfer learning** Since CNF is formulated as a collocation problem with a learnable inductive bias, we can pre-train a set of basis functions with desirable inductive biases, such as well conditioning, smoothness, and more. When the pre-trained basis functions are applied to unseen data, we can directly compute weights with little or no training, as the problem reduces to a close-to-collocation problem. We demonstrate this in solving a partial differential equation on an irregular grid in *inference time* and *without* requiring any training or data; see [Supplementary](#).

**Sparse solver** Taking inspiration from classical reconstruction techniques [23, 40], we introduce a *patch-based* approach that restricts the support of our hybrid kernel function (Eq. 9). This defines a new domain  $\Omega_\sigma \subset \Omega$ , representing the subset of the original domain that possesses support. By carefully selecting the compact support of  $\kappa_G$ , the linear system can be made sufficiently local such that the size of the system to be solved for each  $\mathbf{x} \in \Omega_\sigma$  is controlled to fit within the processor’s memory limitations.

## 4 Applications

For efficient adoption of CNF in real-world applications, we develop a PyTorch framework that abstracts the definition of the basis function, enabling users to conveniently define and experiment with custom architectures. Users can also define an arbitrary linear differential operator by providing a regular expression in  $\LaTeX^2$ . This can be processed to auto-compute the exact value of the function after the operation, thereby eliminating the need for the user to manually execute the operation.

Using this framework, we leverage CNF in four different applications, employing distinct basis functions in each application based on the specific context of the problem. We elucidate and empirically demonstrate the merits of the chosen basis design in each particular scenario. Our intention is to use these examples as a guideline for selecting appropriate basis functions. Apart from Sec. 4.1, which serves as a toy example, we demonstrate unique advantages or state-of-the-art results achieved in each application when employing CNF.

---

<sup>2</sup>For instance, to specify an advection constraint (Eq. 14), the user can pass `f_{x_1} + {beta}f_{x_0}`.

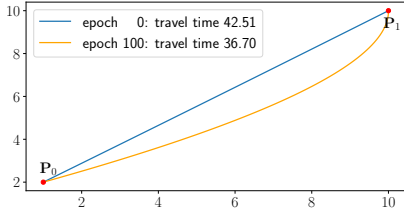


Figure 1: The optical paths and travel time before and after the optimization. The constraints are strictly enforced throughout the optimization.

Table 1: Quantitative comparison of material appearance fitting methods. We evaluate by rendering the learned BRDFs with environment map illumination and computing the mean and standard deviation of image metrics over all materials from the MERL BRDF dataset [21].

	RMSE $\times 10^{-2}$	PSNR	SSIM
NBRDF [35]	1.57 $\pm$ 2.86	44.96 $\pm$ 11.55	.96 $\pm$ .07
FFN [37]	1.16 $\pm$ 1.36	44.72 $\pm$ 10.46	.98 $\pm$ .03
SIREN [34]	3.32 $\pm$ 3.05	33.43 $\pm$ 8.84	.93 $\pm$ .08
Kernel FFN	0.94 $\pm$ 1.16	46.32 $\pm$ 9.92	.98 $\pm$ .03
Kernel SIREN	<b>0.60 <math>\pm</math> 0.54</b>	<b>47.95 <math>\pm</math> 7.99</b>	<b>.99 <math>\pm</math> .01</b>

#### 4.1 Fermat’s Principle

Fermat’s principle in optics states that the path taken by a ray between two given points is the path that can be traveled in the least time. This can be formulated as a constrained optimization problem:

$$\arg \min_{\mathcal{C}} \int_{\mathcal{C}} \frac{ds}{v} \quad \text{s.t.} \quad \partial \mathcal{C} = \{\mathbf{p}_0, \mathbf{p}_1\}, \quad (10)$$

where  $ds$  is the differential arc length that the ray travels along contour  $\mathcal{C}$  and  $v$  is the light speed that varies along the contour due to the refractive index of the medium. The contour’s entry and exit points  $\partial \mathcal{C}$  are hard constraints and the contour is optimized to minimize the travel time  $\int_{\mathcal{C}} \frac{ds}{v}$ . We model the contour  $\mathcal{C}$  as a collection of points from a parametric equation, i.e.  $\mathcal{C} := \{\mathbf{p}(x) := \beta_1 f_1(x) + \beta_2 f_2(x) \mid x \in [0, 1]\}$ . As there are in total two constraints, we use two quadratic polynomials  $\{f_1, f_2\}$  as basis functions. We chose polynomial basis functions due to the simplicity of the problem. The weights  $\{\beta_1, \beta_2\}$  are solved differentially to fit the hard constraints. The coefficients of the polynomials are learnable parameters that can be updated with respect to the loss function. We show the results in Fig. 1 with an increasing refractive index along the Y-axis.

#### 4.2 Learning Material Appearance

In visual computing, the synthesis of realistic renderings fundamentally requires an accurate description of the reflection of light on surfaces [11]. This is commonly expressed by the Bidirectional Reflectance Distribution Function (BRDF), described by Nicodemus *et al.* [24], which quantifies the ratio of incident and outgoing light intensities for a single material:  $f_r(\omega_i, \omega_o)$ , where  $\omega_i, \omega_o \in S^2$  are the incident and outgoing light directions.

Our aim is to learn a neural representation  $\Phi_{\theta}(\omega_i, \omega_o)$  with parameters  $\theta$  that matches the ground truth BRDF  $f_r(\omega_i, \omega_o), \forall \omega_i, \omega_o \in S^2$  as closely as possible. We constrain  $\Phi$  by taking 100 samples  $(\hat{\omega}_i, \hat{\omega}_o)$ , where half of them are sampled uniformly at random, and the other half of  $\hat{\omega}_o$  are concentrated around the direction of the perfect reflection of  $\hat{\omega}_i$ . This means that the latter constraint points are located around the specular highlight, which contains high-frequency details that regular neural networks struggle to learn [32, 31, 19, 35]. We illustrate these issues in Fig. 2, by comparing our Gaussian kernel method (Eq. 7) against multiple SOTA neural-based fitting approaches [34, 37, 35] for efficient uniform BRDF reconstruction. We compare by learning highly specular materials from the MERL BRDF database [21], with size-matching networks for a fair comparison, and rendering a standard fixed scene (for the full set of MERL rendering results, see [Supplementary](#)). Following previous work [35], we train our methods and baselines by sampling 640k sets of  $(\omega_i, \omega_o)$  and minimizing L1 loss in the log domain, to handle the wide range of values due to specular highlights:

$$\begin{aligned} \arg \min_{\theta} \mathbb{E}_{\omega_i, \omega_o} |\Phi_{\theta}(\omega_i, \omega_o) - \log(f_r(\omega_i, \omega_o) + 1)| \\ \text{s.t. } \Phi_{\theta}(\hat{\omega}_i, \hat{\omega}_o) = \log(f_r(\hat{\omega}_i, \hat{\omega}_o) + 1). \end{aligned} \quad (11)$$

We summarize the results computed over all MERL materials in Tab. 1, where we show that our approaches can effectively learn more accurate material appearance than currently existing methods and achieve state-of-the-art performance using SIREN [34] as the encoder network.

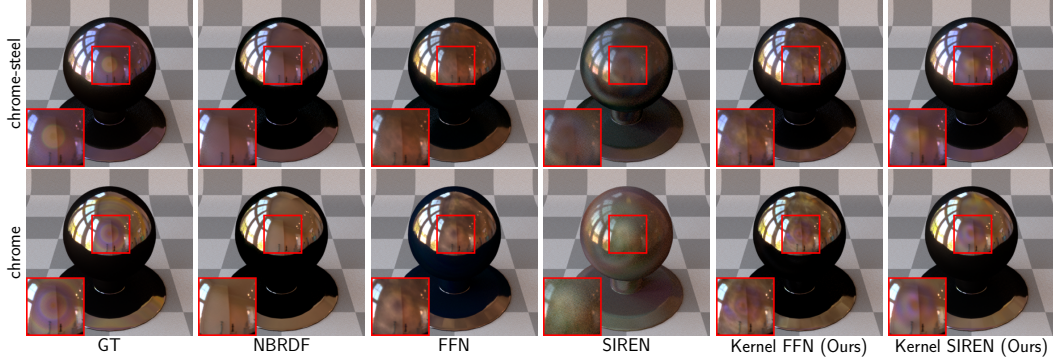


Figure 2: Learned material appearance by enforcing hard constraints around the specular highlights.

### 4.3 Interpolatory Shape Reconstruction

The representation of shapes via neural implicit functions [15] has recently received much attention [28, 2, 34]. Compared to traditional forms of representation like point clouds, meshes, or voxel grids, neural implicit functions offer a flexible and continuous representation, that can handle unrestricted topology. In this section, we demonstrate how our method can be used to enforce exact interpolation constraints on implicit shape representations themselves, while retaining the ability to train the field with geometry specific inductive bias. Given an *oriented* point cloud  $\mathcal{P} := \{(\mathbf{x}_i, \mathbf{n}_i)\}_{i \in I}$ , our aim is to construct a continuous implicit function  $\Phi(\mathbf{x})$  on the domain  $\Omega$  whose 0-level-set  $\mathcal{S} := \{\mathbf{p} \in \Omega \mid \Phi(\mathbf{p}) = 0\}$  represents the surface of the geometry.

**Exact normal constraints** First, we show how our framework can be used to learn an implicit shape representation, while exactly interpolating both points and their associated surface normals. We conduct experiments in 2D, and formulate the constrained field using our hypernetwork kernel architecture (Eq. 8) as it involves higher-order constraints. We constrain the field such that  $\Phi(\mathbf{x}_i) = 0, \forall \mathbf{x}_i \in \mathcal{P}$  and  $\nabla \Phi(\mathbf{x}_i) = \mathbf{n}_i, \forall \mathbf{x}_i, \mathbf{n}_i \in \mathcal{P}$ . Inspired by the geometrically motivated initialization of [2], we use weights that are pretrained to represent the SDF of a circle with the desired number of constraint points. We found this placed the network in a more favorable starting position to produce plausible surfaces under new constraint points. We then train the network to solve the Eikonal equation, via minimizing the quadratic loss function:

$$\mathcal{L} = \mathbb{E}_{\mathbf{x}} (\|\nabla_{\mathbf{x}} \Phi(\mathbf{x})\| - 1)^2, \quad (12)$$

where the expectation is taken with respect to a uniform distribution over the spatial domain  $\Omega$ . The results after training the field are shown in the bottom row of Fig. 3(a). Our method produces plausible surfaces to explain the point cloud, with the advantage of not depending on manufactured offset points to ensure the existence of a non-trivial implicit surface.

**Large-scale constraints** To demonstrate our patch-based sparse solver, we reconstruct 3D point clouds containing 10,000 points, uniformly sampled over the surface. We set the support radius of the hybrid kernel basis (Eq. 9) to four times the average nearest neighbor distance, and we set regions of space with no support to have the constant value of  $10^5$ ; see Fig. 3(b) for results.

### 4.4 Self-tuning PDE Solver

Our approach and framework can also be applied to solve partial differential equations (PDEs). If using fixed radial basis functions (RBFs) without optimization, our method simplifies to the *Kansa method* [18], a type of spectral collocation method where partial derivatives are enforced via hard constraints. One disadvantage of the Kansa method is the difficulty in choosing the appropriate RBF kernel [5]. When using a Gaussian kernel, a large bandwidth may lead to an ill-conditioned system, while a small bandwidth could break the global smoothness of the solution function. This is especially challenging when the number or dimension of collocation points is large or when the points are closely or irregularly spaced, making it difficult to manually fine-tune the hyperparameters of the RBF.

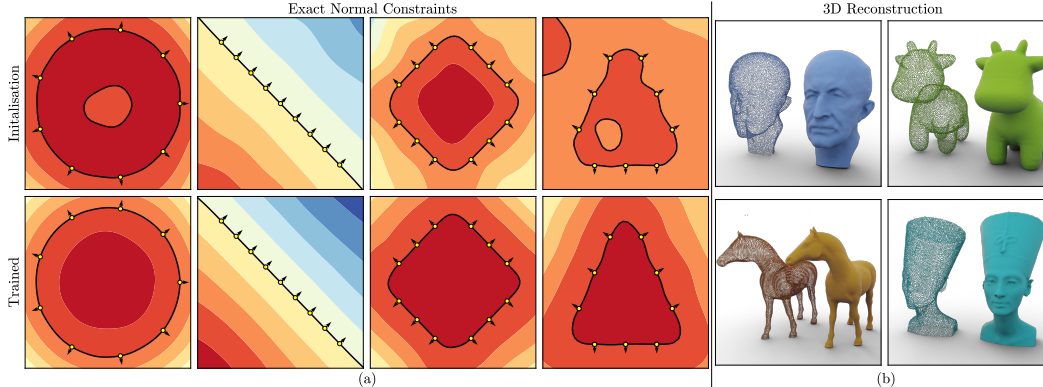


Figure 3: (a): Learning shapes from 2D point clouds (*yellow points*) with oriented normals (*black arrows*) using our method; black lines depict the zero level sets of network. The method interpolates both the point and gradient constraints on initialization and produces a plausible surface after training to minimize the Eikonal constraint over the field. (b): Surface reconstruction of 3D point clouds containing 10,000 points, using our patch-based approach. The reconstruction problem is constrained by the points and pseudo-normal constraints [39, 42] on the points; no training is required to produce smooth surfaces in the dense case.

Our method addresses this limitation by supporting the automatic fine-tuning of hyperparameters, optimizing both the conditioning and global smoothness of the solution:

$$\arg \min_{\theta} \omega_1 \text{cond}(\mathbf{A}_{f_{\theta}}) + \omega_2 \underbrace{\int |\nabla f_{\theta}(\mathbf{x})| d\mathbf{x}}_{\text{total variation}} \quad \text{s.t.} \quad \mathcal{F}_j[f](\mathbf{x}) = g_j(\mathbf{x}) \quad \forall j, \quad (13)$$

where  $\text{cond}(\mathbf{A}_f)$  is the condition number of the linear system and  $\mathcal{F}_j$  corresponds to the PDE constraints along with the initial and boundary conditions. We demonstrate this approach by solving the following 1D advection equation [36] on an irregular grid:

$$\begin{aligned} \frac{\partial u(x,t)}{\partial t} + \beta(x) \frac{\partial u(x,t)}{\partial x} &= 0, & x \in (0,1), t \in (0,1), \\ u(x,t=0) &= u_0(x), & x \in (0,1), \end{aligned} \quad (14)$$

where  $u_0(x)$  represents the initial state of the system. We sampled 32 points on the boundary  $t = 0$  and  $31 \times 32$  points on the space-time domain  $(0,1) \times (0,1)$ , which amount to a total of 1024 points, as hard constraints. The non-boundary samples, shown as *red crosses* in Fig. 4 are generated by a uniform grid perturbed by Gaussian noise. Therefore, we cannot use a single unified RBF bandwidth to fit such an irregular grid. Rather, we design a *skewed radial basis function*,

$$\kappa'_i(\mathbf{x}_i, \mathbf{x}) = \exp\left(-\frac{1}{2}(\mathbf{x} - \mathbf{x}_i)^T \Sigma_i^{-1}(\mathbf{x} - \mathbf{x}_i)\right), \quad (15)$$

where  $\mathbf{x} = (x, t)$  and  $\Sigma_i = \text{diag}([a_i, b_i])$  is a per-basis learnable covariance matrix. Our results in Tab. 2 show that using the skewed RBF kernel and optimizing per-basis parameters consistently improves performance on the irregular grid.

## 5 Summary

We introduce Constrained Neural Fields (CNF), a method that imposes linear operator constraints on deep neural networks, and demonstrate its effectiveness through various real-world applications. Although we restrict the operator to be linear in this work, CNF can be extended to accommodate nonlinear operators by solving a nonlinear version of Eq. 3, provided that the solver is differentiable. This could be accomplished through the use of implicit layers [13], which we leave as future work. Support for nonlinear constraints could unlock a host of intriguing applications, including solving complex PDEs encountered in fields such as physics, engineering, finance, and computer graphics.



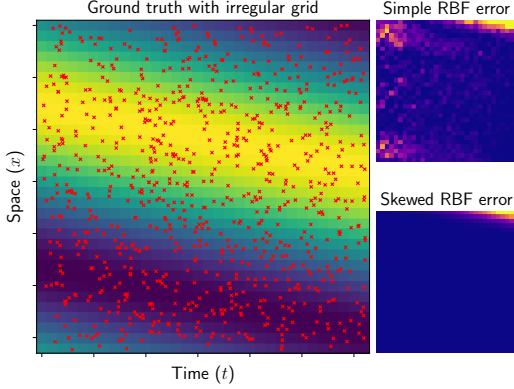


Figure 4: Left: Ground truth advection function and skewed input grid with  $\sigma = 0.1$  perturbation. Right: Error maps for simple and skewed RBF.

Table 2: Solving the 1D advection PDE ( $\beta = 0.1$ ) with a simple (left) and skewed (right) RBF kernel. Both versions were optimized by our framework. We can see the benefit of using the skewed RBF at various perturbation levels.

Perturbation	RBF		Skewed RBF	
	RMSE	nRMSE	RMSE	nRMSE
0.01	0.0086	0.0149	<b>0.0061</b>	<b>0.0116</b>
0.05	0.0252	0.0442	<b>0.0024</b>	<b>0.0043</b>
0.10	0.1484	0.2534	<b>0.0344</b>	<b>0.0651</b>
0.50	0.0170	0.0297	<b>0.0167</b>	<b>0.0282</b>
1.00	0.2830	0.4838	<b>0.0231</b>	<b>0.0365</b>

## References

- [1] K Atkinson, Ivan Graham, and Ian Sloan. Piecewise continuous collocation for integral equations. *SIAM Journal on Numerical Analysis*, 20(1):172–186, 1983.
- [2] Matan Atzmon and Yaron Lipman. Sal: Sign agnostic learning of shapes from raw data. In *Proceedings of the IEEE/CVF Conference on Computer Vision and Pattern Recognition*, pages 2565–2574, 2020.
- [3] Randall Balestrierio and Yann LeCun. Police: Provably optimal linear constraint enforcement for deep neural networks, 2023.
- [4] Jernej Barbič, Marco da Silva, and Jovan Popović. Deformable object animation using reduced optimal control. In *ACM SIGGRAPH 2009 papers*, pages 1–9. 2009.
- [5] Martin D Buhmann. *Radial basis functions: theory and implementations*, volume 12. Cambridge university press, 2003.
- [6] Richard L Burden and J Douglas Faires. Numerical analysis (ninth edition). *Thomson Brooks/Cole*, pages 57–58, 2010.
- [7] Claudio Canuto, M Yousuff Hussaini, Alfio Quarteroni, and Thomas A Zang. *Spectral methods: evolution to complex geometries and applications to fluid dynamics*. Springer Science & Business Media, 2007.
- [8] Anpei Chen, Zexiang Xu, Xinyue Wei, Siyu Tang, Hao Su, and Andreas Geiger. Factor fields: A unified framework for neural fields and beyond, 2023.
- [9] E Ward Cheney and David R Kincaid. *Numerical mathematics and computing*. Cengage Learning, 2012.
- [10] George Cybenko. Approximation by superpositions of a sigmoidal function. *Mathematics of control, signals and systems*, 2(4):303–314, 1989.
- [11] Yue Dong. Deep appearance modelling: A survey. *Visual Informatics*, 3(2):59–68, 2019.
- [12] Priya Donti, David Rolnick, and J Zico Kolter. Dc3: A learning method for optimization with hard constraints. In *International Conference on Learning Representations*, 2021.
- [13] Laurent El Ghaoui, Fangda Gu, Bertrand Travacca, Armin Askari, and Alicia Tsai. Implicit deep learning. *SIAM Journal on Mathematics of Data Science*, 3(3):930–958, 2021.
- [14] Herbert Goldstein. *Classical mechanics*. Addison-Wesley World Student Series, 1950.
- [15] Amos Groppe, Lior Yariv, Niv Haim, Matan Atzmon, and Yaron Lipman. Implicit geometric regularization for learning shapes. *arXiv preprint arXiv:2002.10099*, 2020.
- [16] David Ha, Andrew Dai, and Quoc V Le. Hypernetworks. *arXiv preprint arXiv:1609.09106*, 2016.

- [17] Johannes Hendriks, Carl Jidling, Adrian Wills, and Thomas Schön. Linearly constrained neural networks, 2021.
- [18] Edward J Kansa. Multiquadrics—a scattered data approximation scheme with applications to computational fluid-dynamics—ii solutions to parabolic, hyperbolic and elliptic partial differential equations. *Computers & mathematics with applications*, 19(8-9):147–161, 1990.
- [19] Alexandr Kuznetsov, Krishna Mullia, Zexiang Xu, Miloš Hašan, and Ravi Ramamoorthi. Neu-mip: Multi-resolution neural materials. *Transactions on Graphics (Proceedings of SIGGRAPH)*, 40(4), July 2021.
- [20] Lu Lu, Raphael Pestourie, Wenjie Yao, Zhicheng Wang, Francesc Verdugo, and Steven G Johnson. Physics-informed neural networks with hard constraints for inverse design. *SIAM Journal on Scientific Computing*, 43(6):B1105–B1132, 2021.
- [21] Wojciech Matusik, Hanspeter Pfister, Matt Brand, and Leonard McMillan. A data-driven reflectance model. *ACM Transactions on Graphics*, 22(3):759–769, July 2003.
- [22] Sylvain Meignen and Valérie Perrier. A new formulation for empirical mode decomposition based on constrained optimization. *IEEE Signal Processing Letters*, 14(12):932–935, 2007.
- [23] Bryan S Morse, Terry S Yoo, Penny Rheingans, David T Chen, and Kalpathi R Subramanian. Interpolating implicit surfaces from scattered surface data using compactly supported radial basis functions. In *ACM SIGGRAPH 2005 Courses*, pages 78–es. 2005.
- [24] Fillemon Nicodemus, J C. Richmond, J J. Hsia, I W. Ginsberg, and T L. Limperis. Geometrical considerations and nomenclature for reflection. 160, 10 1977.
- [25] Jorge Nocedal and Stephen J Wright. *Numerical optimization*. Springer, 1999.
- [26] Geoffrey Négiar, Michael W. Mahoney, and Aditi S. Krishnapriyan. Learning differentiable solvers for systems with hard constraints, 2023.
- [27] John G Papastavridis. Analytical mechanics: A comprehensive treatise on the dynamics of constrained systems (reprint edition). 2014.
- [28] Jeong Joon Park, Peter Florence, Julian Straub, Richard Newcombe, and Steven Lovegrove. DeepSDF: Learning continuous signed distance functions for shape representation. In *Proceedings of the IEEE/CVF conference on computer vision and pattern recognition*, pages 165–174, 2019.
- [29] Michael Posa, Cecilia Cantu, and Russ Tedrake. A direct method for trajectory optimization of rigid bodies through contact. *The International Journal of Robotics Research*, 33(1):69–81, 2014.
- [30] Charles R Qi, Hao Su, Kaichun Mo, and Leonidas J Guibas. Pointnet: Deep learning on point sets for 3d classification and segmentation. In *Proceedings of the IEEE conference on computer vision and pattern recognition*, pages 652–660, 2017.
- [31] Gilles Rainer, A. Ghosh, Wenzel Jakob, and T. Weyrich. Unified neural encoding of btfs. *Comput. Graph. Forum*, 39:167–178, 2020.
- [32] Gilles Rainer, Wenzel Jakob, Abhijeet Ghosh, and Tim Weyrich. Neural BTF compression and interpolation. *Computer Graphics Forum (Proc. Eurographics)*, 38(2):1–10, May 2019.
- [33] Szymon Rusinkiewicz. A new change of variables for efficient BRDF representation. In *Rendering Techniques (Proceedings of Eurographics Workshop on Rendering)*, Vienna, Austria, June 1998.
- [34] Vincent Sitzmann, Julien N.P. Martel, Alexander W. Bergman, David B. Lindell, and Gordon Wetzstein. Implicit neural representations with periodic activation functions. In *arXiv*, 2020.
- [35] Alejandro Sztrajman, Gilles Rainer, Tobias Ritschel, and Tim Weyrich. Neural brdf representation and importance sampling. *Computer Graphics Forum*, 2021.
- [36] Makoto Takamoto, Timothy Praditia, Raphael Leiteritz, Daniel MacKinlay, Francesco Alesiani, Dirk Pflüger, and Mathias Niepert. Pdebench: An extensive benchmark for scientific machine learning. *Advances in Neural Information Processing Systems*, 35:1596–1611, 2022.
- [37] Matthew Tancik, Pratul P. Srinivasan, Ben Mildenhall, Sara Fridovich-Keil, Nithin Raghavan, Utkarsh Singhal, Ravi Ramamoorthi, Jonathan T. Barron, and Ren Ng. Fourier features let networks learn high frequency functions in low dimensional domains. *NeurIPS*, 2020.

- [38] Russ Tedrake. *Underactuated Robotics*. 2023.
- [39] Greg Turk and James F O'brien. Shape transformation using variational implicit functions. In *ACM SIGGRAPH 2005 Courses*, pages 13–es. 2005.
- [40] Christian Walder, Bernhard Schölkopf, and Olivier Chapelle. Implicit surface modelling with a globally regularised basis of compact support. In *Computer Graphics Forum*, volume 25, pages 635–644. Amsterdam: North Holland, 1982-, 2006.
- [41] Francis Williams, Zan Gojcic, Sameh Khamis, Denis Zorin, Joan Bruna, Sanja Fidler, and Or Litany. Neural fields as learnable kernels for 3d reconstruction, 2021.
- [42] Francis Williams, Zan Gojcic, Sameh Khamis, Denis Zorin, Joan Bruna, Sanja Fidler, and Or Litany. Neural fields as learnable kernels for 3d reconstruction. In *Proceedings of the IEEE/CVF Conference on Computer Vision and Pattern Recognition*, pages 18500–18510, 2022.
- [43] Suttisak Wizadwongsa, Pakkapon Phongthawee, Jiraphon Yenphraphai, and Supasorn Suwanakorn. Nex: Real-time view synthesis with neural basis expansion, 2021.

# Neural Fields with Hard Constraints of Arbitrary Differential Order

## Supplementary Material

In this supplemental material, we provide additional evaluations of various designs of neural basis functions (Sec. A), along with additional details and results regarding their applications in material appearance learning (Sec. B), interpolatory shape reconstruction (Sec. C), and the self-tuning PDE solver (Sec. D) which includes a *transfer learning* example (Sec. D.2).

### A Neural Basis Functions

#### A.1 Issues with the Neural Kernel Basis Function

We illustrate how, when using the neural kernel basis function (Eq. 7), enforcing multiple linear operator constraints at the same anchor point would result in *repeated* basis functions  $\Psi_i \equiv \Psi_j \equiv \kappa(\phi(\mathbf{x}_{\text{anchor}}), \phi(\mathbf{x}))$ , consequently leading to an *ill-conditioned* linear system. Recall Eq. 6:

$$\begin{bmatrix} \mathcal{F}_1[\Psi_1](\mathbf{x}_1^1) & \mathcal{F}_1[\Psi_2](\mathbf{x}_1^1) & \cdots \\ \mathcal{F}_1[\Psi_1](\mathbf{x}_2^1) & \mathcal{F}_1[\Psi_2](\mathbf{x}_2^1) & \cdots \\ \vdots & \vdots & \ddots \\ \mathcal{F}_2[\Psi_1](\mathbf{x}_1^2) & \mathcal{F}_2[\Psi_2](\mathbf{x}_1^2) & \cdots \\ \mathcal{F}_2[\Psi_1](\mathbf{x}_2^2) & \mathcal{F}_2[\Psi_2](\mathbf{x}_2^2) & \cdots \\ \vdots & \vdots & \ddots \end{bmatrix} \begin{bmatrix} \beta_1^1 \\ \beta_2^1 \\ \vdots \\ \beta_1^2 \\ \beta_2^2 \\ \vdots \end{bmatrix} = \begin{bmatrix} g_1(\mathbf{x}_1^1) \\ g_1(\mathbf{x}_2^1) \\ \vdots \\ g_2(\mathbf{x}_1^2) \\ g_2(\mathbf{x}_2^2) \\ \vdots \end{bmatrix}, \quad (16)$$

where  $\mathbf{x}_n^j$  indicates the  $n$ -th point in  $\mathcal{S}_j$  such that  $\mathcal{F}_j[f](\mathbf{x}) = g_j(\mathbf{x}), \forall \mathbf{x} \in \mathcal{S}_j$ . When applying the neural kernel basis function  $\Psi_i(\mathbf{x}) = \kappa(\phi(\mathbf{x}_i), \phi(\mathbf{x})) = \kappa_N(\mathbf{x}_i, \mathbf{x})$ , the above matrix equation becomes:

$$\begin{bmatrix} \mathcal{F}_1 \kappa_N(\mathbf{x}_1^1, \mathbf{x}_1^1) & \mathcal{F}_1 \kappa_N(\mathbf{x}_2^1, \mathbf{x}_1^1) & \cdots \\ \mathcal{F}_1 \kappa_N(\mathbf{x}_1^1, \mathbf{x}_2^1) & \mathcal{F}_1 \kappa_N(\mathbf{x}_2^1, \mathbf{x}_2^1) & \cdots \\ \vdots & \vdots & \ddots \\ \mathcal{F}_2 \kappa_N(\mathbf{x}_1^2, \mathbf{x}_1^2) & \mathcal{F}_2 \kappa_N(\mathbf{x}_2^2, \mathbf{x}_1^2) & \cdots \\ \mathcal{F}_2 \kappa_N(\mathbf{x}_1^2, \mathbf{x}_2^2) & \mathcal{F}_2 \kappa_N(\mathbf{x}_2^2, \mathbf{x}_2^2) & \cdots \\ \vdots & \vdots & \ddots \end{bmatrix} \begin{bmatrix} \beta_1^1 \\ \beta_2^1 \\ \vdots \\ \beta_1^2 \\ \beta_2^2 \\ \vdots \end{bmatrix} = \begin{bmatrix} g_1(\mathbf{x}_1^1) \\ g_1(\mathbf{x}_2^1) \\ \vdots \\ g_2(\mathbf{x}_1^2) \\ g_2(\mathbf{x}_2^2) \\ \vdots \end{bmatrix}, \quad (17)$$

Without loss of generality, assuming  $f : \mathbb{R} \mapsto \mathbb{R}$ ;  $\mathcal{F}_1$  is identity map;  $\mathcal{F}_2$  is differentiation; and  $\mathcal{S}_1 = \mathcal{S}_2 = \{x_0\}$  (same anchor point for both constraints), the matrix equation reduces to:

$$\underbrace{\begin{bmatrix} \kappa_N(x_0, x_0) & \kappa_N(x_0, x_0) \\ \kappa'_N(x_0, x_0) & \kappa'_N(x_0, x_0) \end{bmatrix}}_{\text{singular}} \begin{bmatrix} \beta_1 \\ \beta_2 \end{bmatrix} = \begin{bmatrix} g_1(x_0) \\ g_2(x_0) \end{bmatrix}. \quad (18)$$

Therefore, the system is ill-conditioned as the matrix has repeated columns. NKF [41] uses this basis function with a dot-product kernel and thus cannot enforce hard constraints simultaneously on both the points and their normals in shape reconstruction, which we further evaluate in Sec. C.1.1. We also discovered significant disadvantages of using a dot-product kernel as opposed to a Gaussian kernel. We elaborate on these findings in Sec. A.2 and Sec. B.2.

#### A.2 Basis Function Ablation

Choosing the appropriate basis function for an application requires consideration of two fundamental properties of basis functions: their linear independence and learning capacity. Linear independence is crucial for satisfying hard constraints, whereas learning capacity is key for fitting the inductive bias. In this ablation study, we train various neural basis functions discussed in Sec. 3.2 to regularize the condition number of the matrix  $\mathbf{A}_f$ , which is used to constrain a 2D function over 4096 points. A large condition number often corresponds to a substantial error in satisfying hard constraints. This study offers insights into how each design is prone to the ill-conditioning of the linear system. For a fair comparison, we use the same architecture for all neural encoders—a 2-layer MLP with Tanh activations and a total of 1.3M trainable parameters.

As shown in Fig. 5, the Gaussian kernel basis is well-conditioned throughout training, while all other methods struggle to reduce the condition number.

In Sec. B.2, we also discovered that the Gaussian kernel basis, when constrained, exhibits the superior learning capacity for fitting the BRDF. In contrast, the performance of other methods was found to be extremely poor. Note that the dot-product kernel and the constrained layer are the basis functions used in [41] and [26], respectively. Based on our findings, we strongly recommend employing the Gaussian kernel basis function when performing constrained optimization for neural fields.

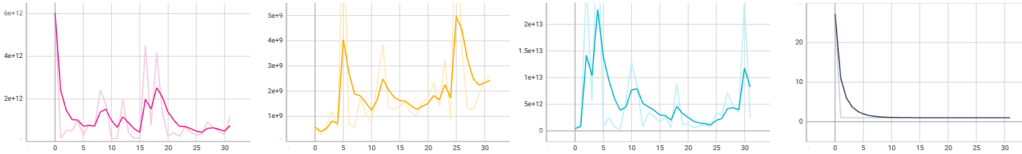


Figure 5: Condition number of different neural basis functions in the following order (left to right): constraint layer (pink), hypernet basis (yellow), dot-product kernel (blue), and Gaussian kernel (black) throughout training.

## B Learning Material Appearance

### B.1 Experiment Details

In the experiments on material appearance fitting, all neural networks have a single hidden layer and we controlled the network width so that all methods have roughly 200k parameters for a fair comparison. Both baseline FFN and kernel FFN use a frequency of 16, meaning that the inputs are mapped to encodings of size 38 before feeding to the MLP. The kernel FFN model uses FFN as an encoder which has a width of 248 and outputs a latent vector of dim 512. The baseline FFN MLP has a width of 718. The kernel SIREN model has a width of 256 and also outputs a latent vector of size 512. The baseline SIREN and NBRDF have a width of 442. We use Adam optimizer with a learning rate of  $5 \times 10^{-4}$  for all methods except for SIREN baseline and kernel SIREN, which use a learning rate of  $1 \times 10^{-4}$  for more stable performance.

For constraint points, we sample the angles  $\theta_h$ ,  $\theta_d$  and  $\phi_d$  as in Rusinkiewicz’s parameterization [33]. A figure of those angles is shown in Fig. 6. We sample  $\theta_d$  and  $\phi_d$  uniformly at random within range  $[0, \pi/2]$  and  $[0, 2\pi]$  respectively. Half of the  $\theta_h$  are also sampled uniformly at random within  $[0, \pi/2]$ , whereas the other half are sampled from a Gaussian distribution with a mean of 0 and a standard deviation of 0.1. Those angles are then converted to 6D in-going and out-going directions as inputs to the networks.

### B.2 Ablation Studies

In Tab. 3 and Fig. 7, we report the ablation results of fitting the BRDF with constraints, including the dot-product kernel using SIREN as the encoder, the hypernet basis with SIREN as the main network, and the constrained layer integrated into SIREN. The hypernet basis uses a SIREN that has a width of 442 as the main network, and a ReLU MLP with one hidden layer with 100 nodes as the hypernetwork. The constraint layer has a width of 319. The hypernet basis and constraint layer produce extremely poor results and are completely unable to perform this task. While the dot-product kernel performs better than both the hypernet basis and the constraint layer, it still significantly underperforms when compared to the Gaussian kernel.

### B.3 Full Results

The complete rendering results for all materials included in the MERL dataset [21] are shown in Fig. 9, Fig. 10, Fig. 11, Fig. 12, Fig. 13 and Fig. 14. We also show the SSIM errors along with the renderings.

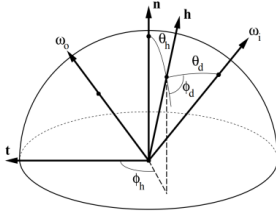


Figure 6: Angles for sampling constraint points for material learning. Figure from [33].

Table 3: Ablations on material appearance learning task. All methods here are based on SIREN [34].

	RMSE $\times 10^{-2}$	PSNR	SSIM
Hypernet Basis	39.02 $\pm$ 16.92	9.74 $\pm$ 6.41	0.70 $\pm$ 0.06
Dot-product Kernel	9.49 $\pm$ 11.32	28.33 $\pm$ 13.22	0.86 $\pm$ 0.13
Constraint Layer	41.85 $\pm$ 14.14	8.37 $\pm$ 4.37	0.70 $\pm$ 0.06
Gaussian Kernel	<b>0.60 <math>\pm</math> 0.54</b>	<b>47.95 <math>\pm</math> 7.99</b>	<b>0.99 <math>\pm</math> 0.01</b>

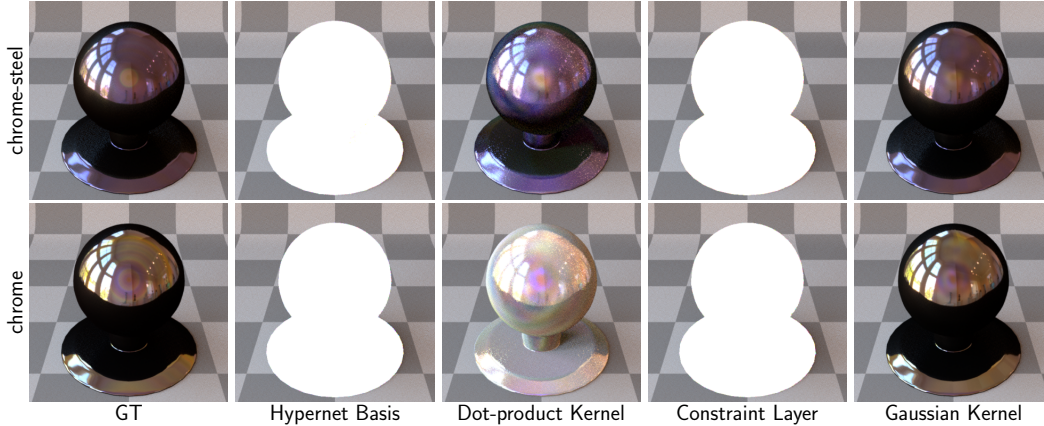


Figure 7: Ablation on the material appearance fitting.

## C Interpolatory Shape Reconstruction

### C.1 Experiment Details

#### C.1.1 Exact Normal Interpolation

In the experiments on exact normal interpolation, the shapes are represented by the level sets of our hypernet kernel. The encoder of our hypernet is constructed of an MLP, which has a single hidden layers containing 1200 hidden units. Between each layer we use a softplus activation, with  $\beta = 10$  and the encoder maps to a feature space of size 800. We use a Gaussian kernel which is initialized with a standard deviation of 50. For all experiments shown, we use a maximum of 50 epochs, a learning rate of  $10^{-5}$ , and the Adam optimizer. To extract the zero-order level set of the implicit representation we use the *Marching Cubes* algorithm, on a uniform grid sampled at a step size of  $1/60$ . For all shapes except the circle, we pretrain the weights of the hypernet encoder to first represent a circle with uniformly sampled constraints equal to the number of constraints of the target shape. The Eikonal loss function defined in Eq. 12 is defined on the domain  $\Omega = [-2, 2] \times [-2, 2]$ , and at each iteration we use 1000 points randomly sampled from  $\Omega$ .

#### C.1.2 Large Scale Constraints

In the demonstration of our *patched-based* approach, we reconstruct point clouds with 10,000 uniformly sampled points. Our current implementation of the patch-based solver doesn't support the hypernet kernel, so we regularize the reconstruction problem using a finite difference scheme [39, 42] and impose the point constraints of  $\Phi(\mathbf{x}_i + \varepsilon \mathbf{n}_i) = \varepsilon$  and  $\Phi(\mathbf{x}_i - \varepsilon \mathbf{n}_i) = -\varepsilon$ , where we set  $\varepsilon = 0.01$  for all reconstructions. As well as the tunable support size, our implementation also places a hard limit on the total number of constraints that are considered for each query point; for all experiments we limit the nearest neighborhood size to 60. Furthermore, as our current implementation does not support tensor batching, the run-time for the patch-based approach, with a marching cubes grid resolution of  $[160 \times 160 \times 160]$ , is approximately 8 hours.

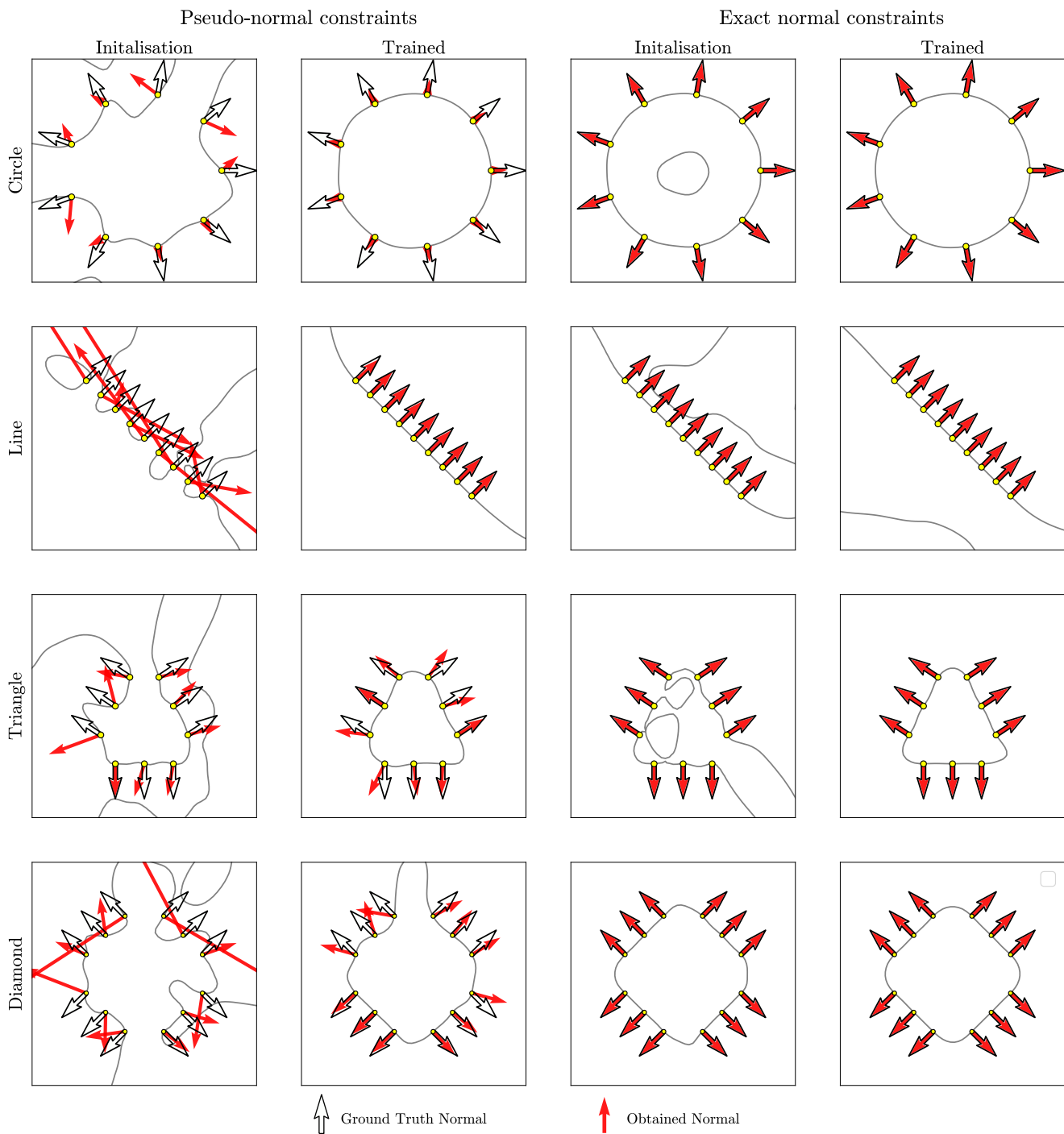


Figure 8: We assess the effectiveness of our precise normal interpolation technique for shape representation. We present the normal vector of the encoded implicit surface (red arrow) before and after training to minimize an Eikonal constraint, for fields bound by pseudo-normal constraints and our exact constraint method. We compare with the ground-truth shape normal vectors (black arrow); our approach produces a surface that faithfully represents both the constraint points and the constraint normal vector.

## C.2 Evaluation of Normal Interpolation

To evaluate the merit of our normal interpolation approach for shape representation, we compare shape representation using our exact gradient constraints and pseudo-normal constraints as used in [41]. We use the same hypernet kernel approach for all experiments, with the same training setup as Sec. C.1.1, except that we do not pretrain the hypernet encoder to represent a circle. For the pseudo-normal constraints, we set the value of  $\epsilon = 0.1$ .

In Fig. 8 we show a visual comparison between the reconstructions achieved when using pseudo-normal constraints and exact gradient constraints. To quantitatively assess each approach we also report the mean normal error:

$$\mathcal{E}_n = \frac{1}{N} \sum_{i=1}^N \|\mathbf{n}(\mathbf{x}_i) - \hat{\mathbf{n}}(\mathbf{x}_i)\|, \quad (19)$$

where  $\mathbf{n}(\mathbf{x}_i) = \nabla_{\mathbf{x}} \Psi(\mathbf{x}_i)$  and  $\hat{\mathbf{n}}(\mathbf{x}_i)$  is the ground truth normal value at  $\mathbf{x}_i$ . The results are tabulated in Table 4.

	Pseudo-normal (†)	Pseudo-normal (*)	Exact normal (†)	Exact normal (*)
Circle	0.776	0.499	$4.516 \times 10^{-6}$	$1.083 \times 10^{-6}$
Line	3.817	$1.589 \times 10^{-2}$	$2.737 \times 10^{-6}$	$6.963 \times 10^{-6}$
Triangle	0.466	0.238	$7.371 \times 10^{-5}$	$6.292 \times 10^{-6}$
Diamond	1.588	0.277	$1.450 \times 10^{-5}$	$3.368 \times 10^{-6}$

Table 4: Evaluation of error in the normal vector of the implicit field, as defined in Eq. 19. The symbols † and \* refer to measurements taken on initialization and after training the field, respectively.

As is evident both from our qualitative visualization and quantitative evaluation, CNF is able to impose exact normal constraints on neural implicit surfaces (to within floating point accuracy).

## D Self-tuning PDE Solver

### D.1 Experiment Details

We selected 1D advection (described in Eq. 14 in Sec. 4.4) as a demonstration of the effectiveness of CNF in solving partial differential equations (PDEs). This choice was made due to its simple, linear form. Additionally, one of the advantages is that the ground truth function has a convenient analytical expression, eliminating the need for iterative solvers for validation. Specifically, our objective is to recover the following function:

$$u(x, t) = \sin 2\pi(x - \beta t), \quad x \in (0, 1), \quad t \in (0, 1). \quad (20)$$

### D.2 Transfer Learning

In Sec. 4.4, we detail how CNF can automatically fine-tune the hyperparameters of the skewed RBF on an irregular grid. Here, we illustrate that, given optimized hyperparameters of the skewed RBF for a particular grid, we can employ the resulting skewed RBF to directly solve a different advection equation (such as a different initial condition) at inference time, without additional training, if the grid remains the same.

For demonstration, we incrementally add a shift,  $\mu$ , to the initial condition of the advection equation, starting from small to large shifts:

$$u_0(x) = \sin(2\pi x) + \mu, \quad x \in (0, 1). \quad (21)$$

The hyperparameters of the skewed RBFs were trained solely when  $\mu = 0$ . When the initial condition,  $u_0(x)$ , is shifted, the new advection equation can be solved with the same kernel at inference time. No further training was conducted; see Tab. 5 for the results.



Table 5: Demonstration of transfer learning with the skewed RBF kernels. The kernels were initially trained exclusively for a 1D advection function with no shift (first row). Subsequently, their transfer learning capabilities were tested at varying shifts. No training was conducted other than for the first row.

Shift $\mu$	Random init Skewed RBF		Pre-trained Skewed RBF	
	RMSE	nRMSE	RMSE	nRMSE
0	0.0127	0.0227	<b>0.0070</b>	<b>0.0129</b>
1	0.0460	0.0736	<b>0.0049</b>	<b>0.0074</b>
10	0.5788	0.0594	<b>0.0177</b>	<b>0.0018</b>
100	5.8613	0.0587	<b>0.2221</b>	<b>0.0022</b>
1000	60.143	0.0602	<b>2.3113</b>	<b>0.0023</b>
10000	635.78	0.0636	<b>23.844</b>	<b>0.0024</b>

The efficacy of this approach can be explained by our perspective of formulating the constrained optimization problem as a collocation problem with learnable inductive bias. Once the preferred inductive bias away from the collocation points is obtained, solving a PDE at the same collocation points is reduced to a pure collocation problem, which requires minimal to no further training.

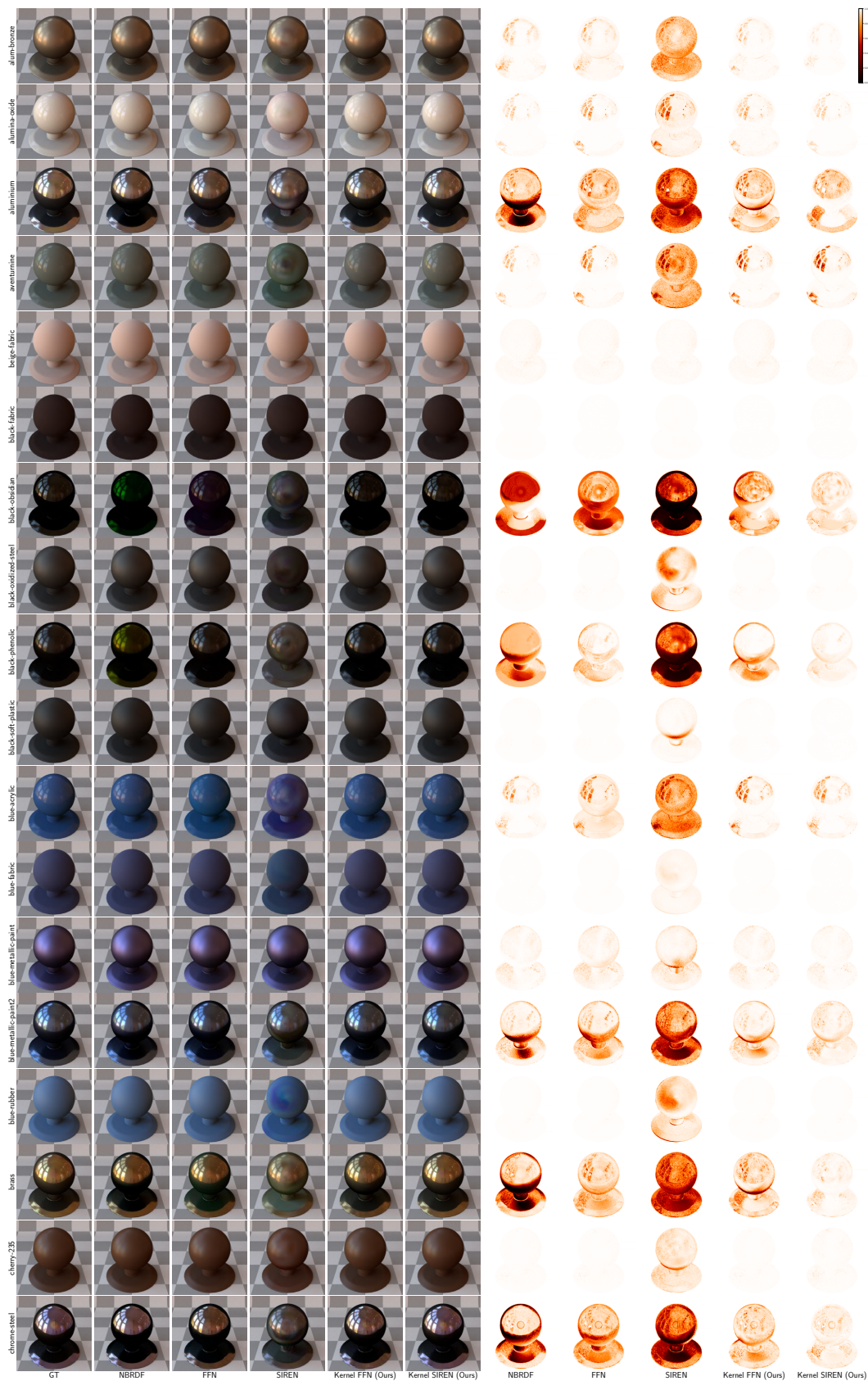


Figure 9: Learned material appearance.

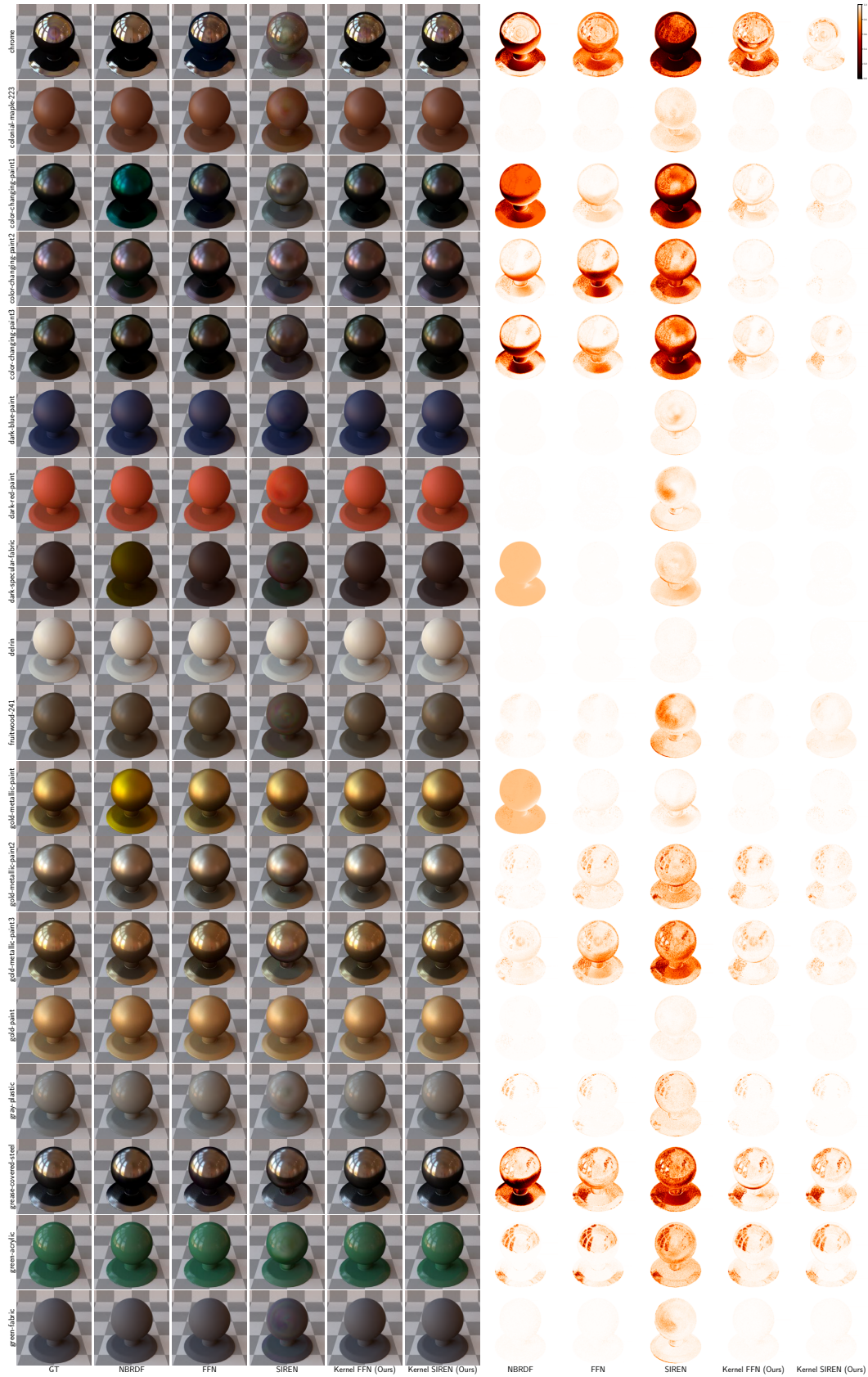


Figure 10: Learned material appearance.

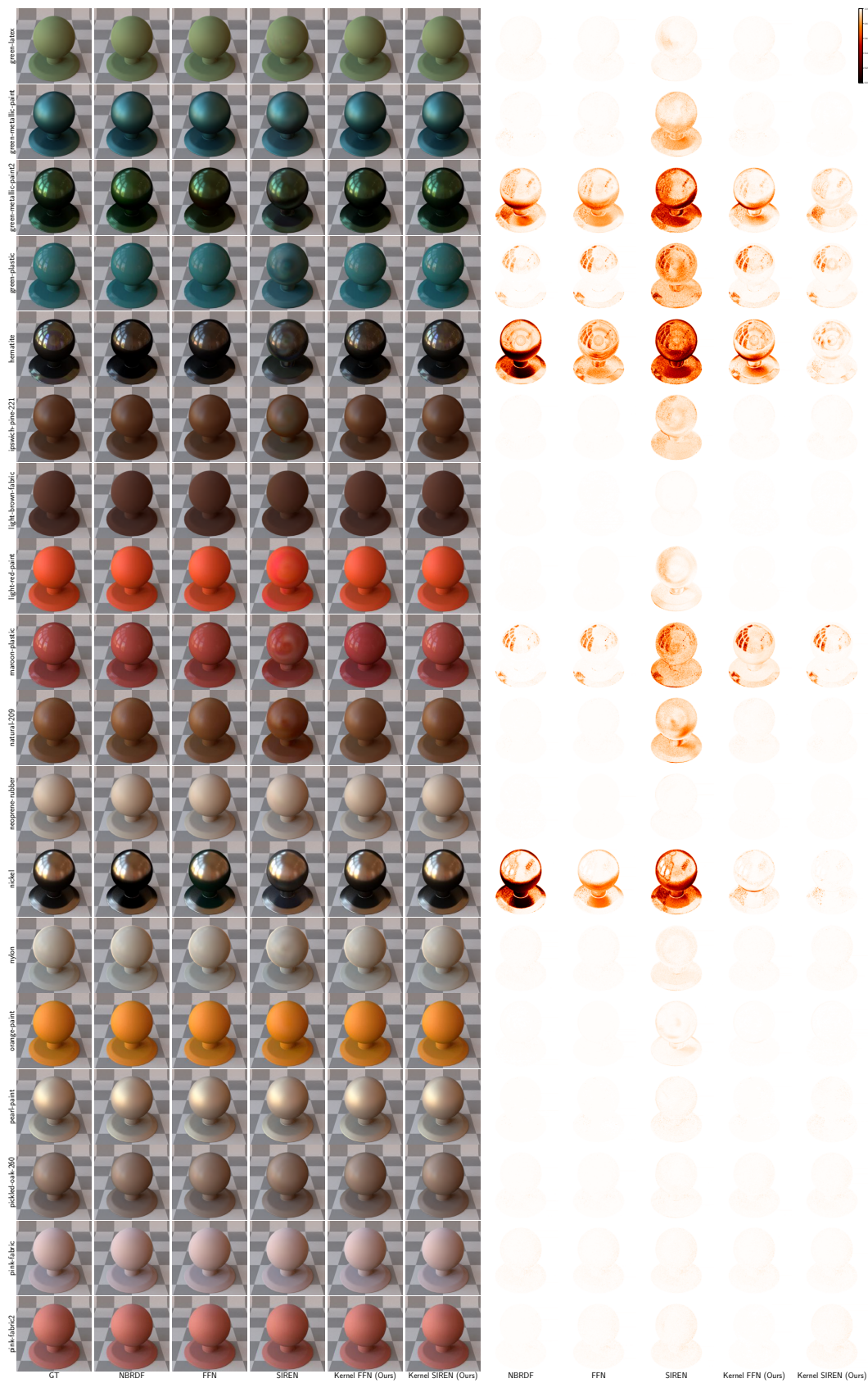


Figure 11: Learned material appearance.

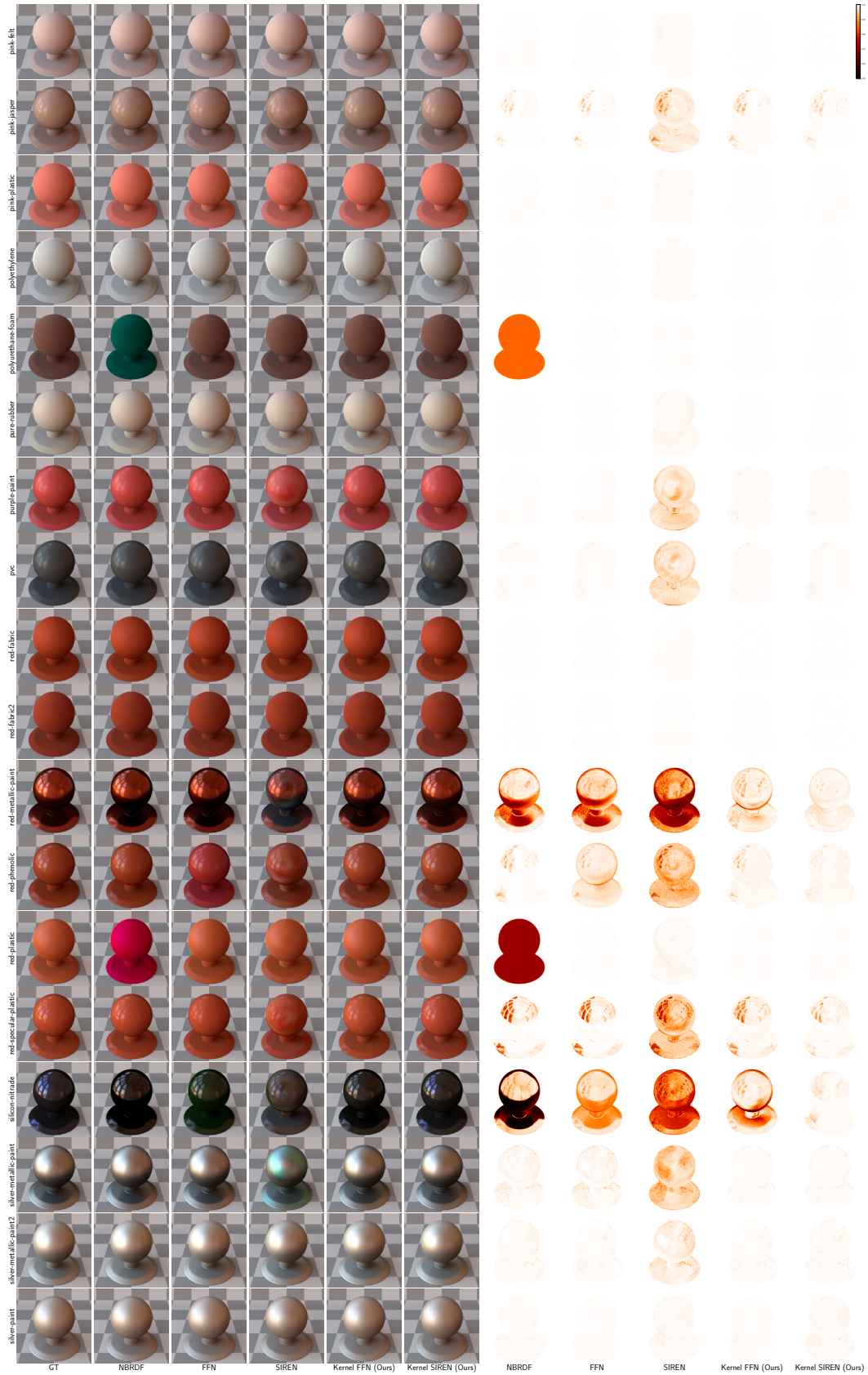


Figure 12: Learned material appearance.

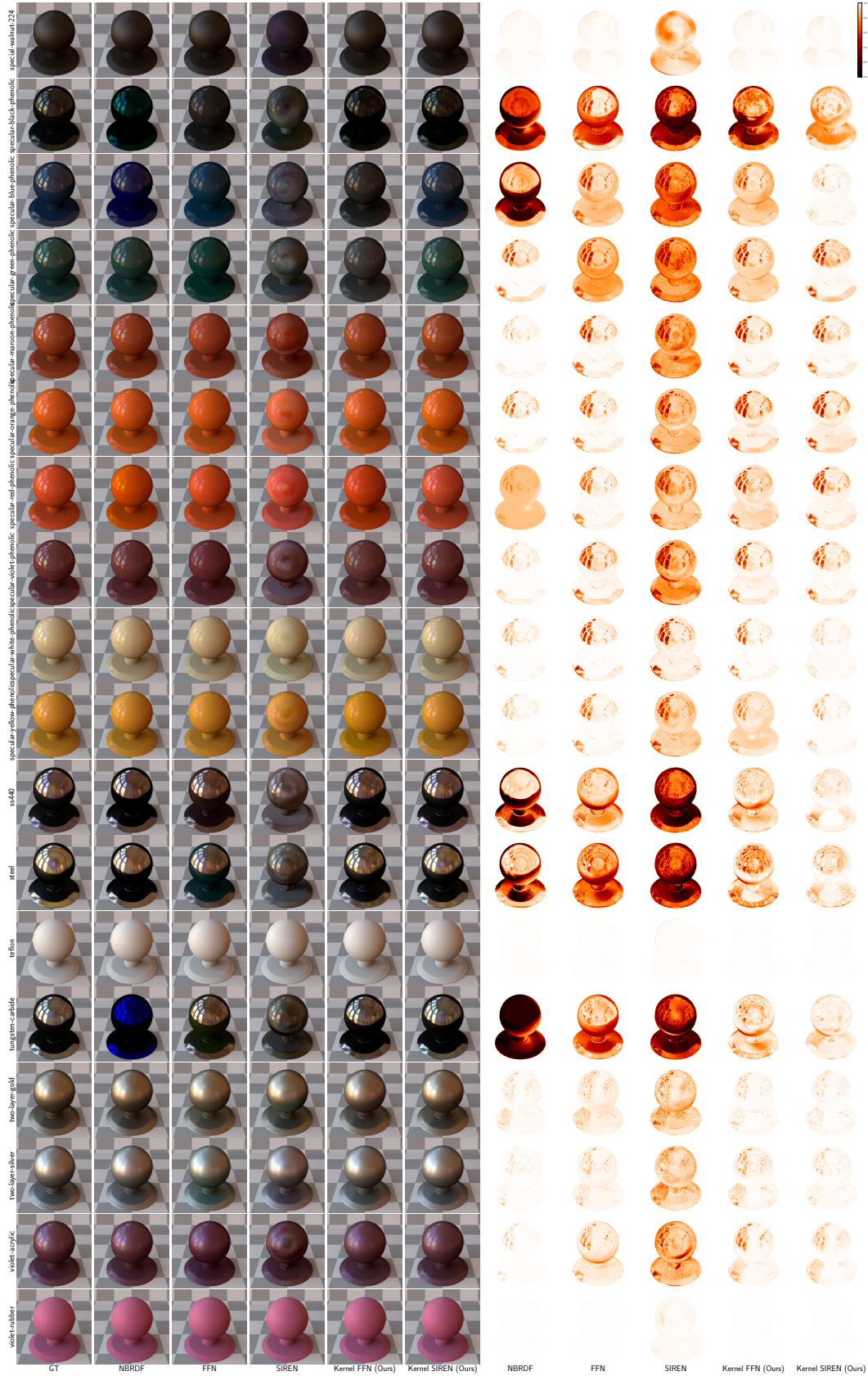


Figure 13: Learned material appearance.

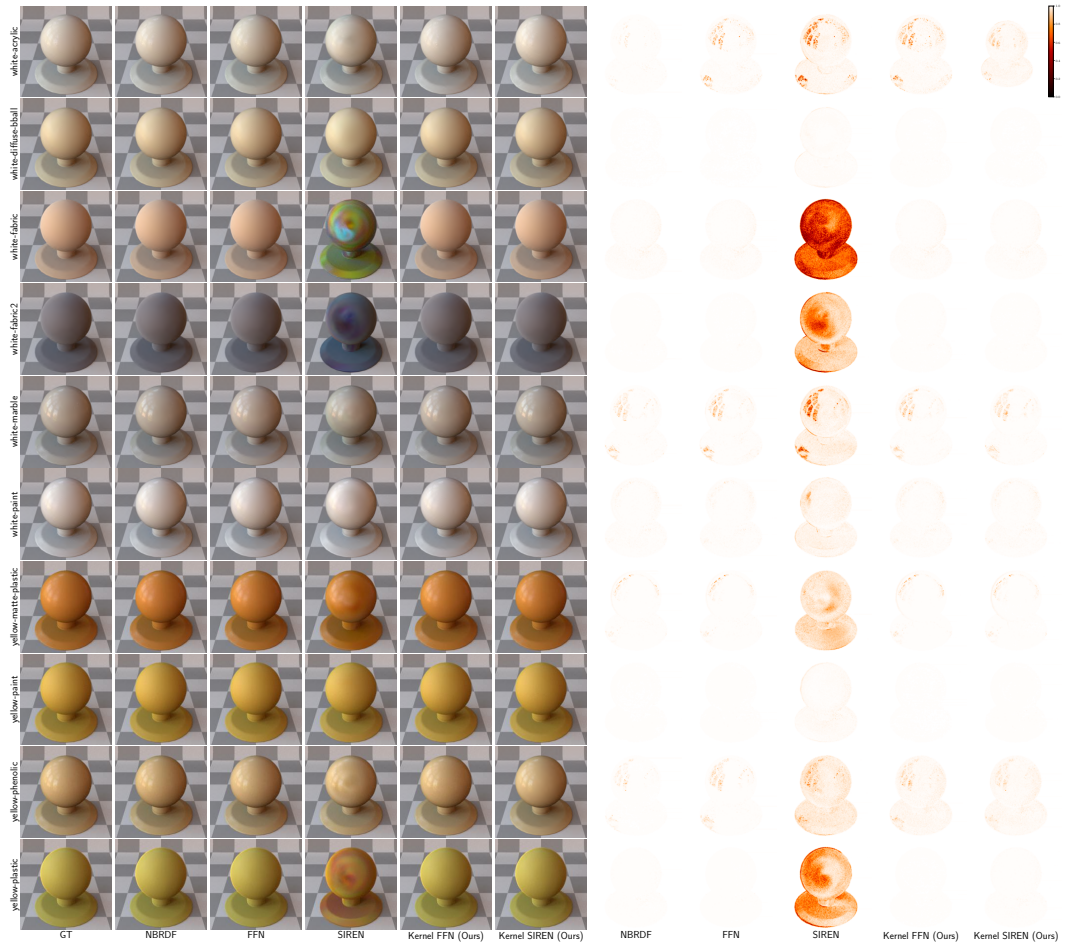


Figure 14: Learned material appearance.